Science Arts & Métiers (SAM)

is an open access repository that collects the work of Arts et Métiers Institute of Technology researchers and makes it freely available over the web where possible.

This is an author-deposited version published in: https://sam.ensam.eu
Handle ID: .http://hdl.handle.net/10985/13135

To cite this version :

Mohamed BEN BETTAIEB, Farid ABED-MERAIM - Ductility prediction of substrate-supported metal layers based on rate-independent crystal plasticity theory - International Journal of Material Forming - Vol. 12, n°2, p.241-255 - 2019

Any correspondence concerning this service should be sent to the repository Administrator : scienceouverte@ensam.eu

Arts et Métiers Institute of Technology

Science Arts & Métiers (SAM)

is an open access repository that collects the work of Arts et Métiers ParisTech researchers and makes it freely available over the web where possible.

This is an author-deposited version published in: http://sam.ensam.eu
Handle ID: .http://hdl.handle.net/null

To cite this version :

Mohamed BEN BETTAIEB, Farid ABED-MERAIM - Ductility prediction of substrate-supported metal layers based on rate-independent crystal plasticity theory - International Journal of Material Forming p.1-15 - 2018

Any correspondence concerning this service should be sent to the repository Administrator : archiveouverte@ensam.eu

Ductility prediction of substrate-supported metal layers based on rate-independent crystal plasticity theory

Mohamed Ben Bettaieb [1,2] & Farid Abed-Meraim [1,2]

Abstract

In several modern technological applications, the formability of functional metal components is often limited by the occurrence of localized necking. To retard the onset of such undesirable plastic instabilities and, hence, to improve formability, elastomer substrates are sometimes adhered to these metal components. The current paper aims to numerically investigate the impact of such elastomer substrates on the formability enhancement of the resulting bilayer. To this end, both the bifurcation theory and the initial imperfection approach are used to predict the inception of localized necking in substrate-supported metal layers. The full-constraint Taylor scale-transition scheme is used to derive the mechanical behavior of a representative volume element of the metal layer from the behavior of its microscopic constituents (the single crystals). The mechanical behavior of the elastomer substrate follows the neo-Hookean hyperelastic model. The adherence between the two layers is assumed to be perfect. Through numerical simulations, it is shown that bonding an elastomer layer to a metal layer allows significant enhancement in formability, especially in the negative range of strain paths. These results highlight the benefits of adding elastomer substrates to thin metal components in several technological applications. Also, it is shown that the limit strains predicted by the initial imperfection approach tend towards the bifurcation predictions as the size of the geometric imperfection in the metal layer reduces.

Keywords Substrate-supported metal layers · Forming limit diagrams · Localized necking · Neo-Hookean model · Rate-independent crystal plasticity · Bifurcation and imperfection analyses

Introduction

Ductile failure is the main mechanism that limits the formability of thin metal sheets during forming processes; therefore, this phenomenon is central in structural integrity assessment together with corrosion and fatigue. Several possible failure scenarios, or mechanisms, may occur during forming operations. In this field, one can quote at least three main scenarios. The first one takes place only for very pure metals. In this case, thin metal sheets fail without the occurrence of damage, owing to the absence of void nucleation sites. In such circumstances, the deformation state is homogeneous at the beginning of the loading and, at a certain limit strain, the deformation starts concentrating in narrow bands. The emergence of such bands marks the development of localized necking in the sheet. The second scenario corresponds to the localization of plastic strain into shear bands owing to various possible softening mechanisms. Subsequently, following the accumulation of large plastic strains and the increase of stress triaxiality in the necked regions, voids nucleate, grow and coalesce to produce final material separation. The third mechanism involves damage nucleation in the material prior to plastic strain localization. The softening induced by the accumulated porosity is sufficient to counteract the strain hardening capacity of the material and leads to plastic strain localization in narrow bands. An extensive study of the different failure mechanisms and the competition between them has been reported in [1]. In the current contribution, we assume that the failure of the studied sheet metals is only due to localized necking, without prior occurrence of damage. For interested readers, an exhaustive academic presentation of the prediction of failure in metallic materials, based on advanced damage models, can be found in [2]. It is now well-

* Mohamed Ben Bettaieb
Mohamed.BenBettaieb@ensam.eu

[1] LEM3, UMR CNRS 7239, Arts et Métiers ParisTech, 4 rue Augustin Fresnel, 57078 Metz Cedex 3, France

[2] DAMAS, Laboratory of Excellence on Design of Alloy Metals for low-mAss Structures, Université de Lorraine, Lorraine, France

recognized that the accurate prediction of the limit strains that lead to localized necking is crucial for designing functional or structural components used in industrial devices. To this end, several numerical models have been developed for the prediction of localized necking, and the associated limit strains are represented in terms of the so-called forming limit diagram (FLD). This FLD concept was originally introduced by Keeler and Backofen [3], for representing the limit strains in the range of positive strain paths, and has been extended by Goodwin [4] to the range of negative strain paths. Over the last decades, two major challenges, related to the formability of metallic components, have been extensively studied both from academic and industrial points of view. The first issue is of scientific nature and is associated with the accurate prediction of the formability limit of the studied material, while the second, of practical nature, is related to the development of industrial solutions to improve its formability.

To solve the first issue, related to the accurate determination of formability limits, several experimental methods have been developed and widely used in both academic and industrial environments. Unfortunately, the use of these experimental techniques has been limited by various practical difficulties, such as the high cost of the experimental tests required for characterizing an FLD. To avoid these difficulties, several analytical and numerical approaches have been set up in the literature as alternatives to the experimental characterization of FLDs (see, e.g., [5, 6]). These alternative approaches require the use of a criterion, to predict the occurrence of strain localization, along with a constitutive model to describe the evolution of the mechanical state of the studied material. Despite their good predictive capabilities, the phenomenological constitutive models, which are the most widely used for the numerical prediction of FLDs, are not able to properly account for some essential physical and mechanical features, such as initial and induced textures and other microstructure-related parameters (crystallographic structure, dislocation motion, initial morphology of grains, slip on crystallographic planes ...). These limitations represent the main motivation behind the more recent use of micromechanical modeling for FLD prediction. The advantage of such physically-based modeling, compared to phenomenological approaches, is its ability to link, in a natural and explicit way, the material microstructure to the formability of the studied sheets. Due to this major advantage, a micromechanical approach is adopted in the current paper to model the mechanical behavior of a small volume element, which is assumed to be representative of the studied metal sheet. The constitutive law of this representative volume element (RVE) is determined from that of its microscopic constituents (the single crystals) by using the full-constraint Taylor scale-transition scheme. The mechanical behavior at the single crystal scale is described by a finite strain rate-independent constitutive model, in which the Schmid law is used to govern the plastic flow. This rate-independent formulation is more suitable for the modeling and the simulation of cold forming processes, where viscous effects are limited. The developed model is applied in the current study to single crystals with FCC crystallographic structure. In order to predict the onset of localized necking, the polycrystalline constitutive model, based on the full-constraint Taylor scheme, is coupled with two different localization criteria: the bifurcation theory, originally developed by Rice [7], and the imperfection approach initiated by Marciniak and Kuczynski [8]. Note that coupling these localization criteria (especially the Marciniak and Kuczynski approach) with the Taylor multiscale scheme is a very challenging problem, from a numerical point of view. Hence, the algorithmic aspects related to this coupling are detailed in the current paper. The use of the Taylor model, instead of other more elaborate (and more complex) multiscale schemes, such as the CPFEM model or the self-consistent approach, allows a considerable reduction in the CPU time required to determine a complete FLD (especially within the initial imperfection approach). However, it is well known that the Taylor multiscale scheme predicts high stress values compared to the self-consistent scheme.

To solve the above-mentioned second issue, related to the improvement of formability of industrial components, a number of technological solutions have been proposed and used in various industrial applications. One of the most-widely used solutions consists in perfectly bonding an elastomer substrate to the original metal component. This technological solution has proven its effectiveness in the improvement of formability of industrial devices [9–13]. For instance, in the design of electronic devices that require high stretchability levels, substrate-supported metal layers are being increasingly used. This is the case of stretchable conductors used in biomedical applications, as well as interconnects that are used in large-scale integrated circuits [9, 10]. The bifurcation theory and the initial imperfection approach, previously developed for the case of freestanding metal layers, are extended here to predict the formability of substrate-supported metal layers. The aim of this extension is to numerically investigate the impact of the addition of an elastomer substrate on the formability of the resulting metal/elastomer bilayer. Note that the formability of substrate-supported metal layers has been studied in very few numerical investigations in the past (see, e.g., [13, 14]). In addition, in these earlier contributions, only phenomenological constitutive models have been used to describe the mechanical behavior of the metal layer. To the authors' best knowledge, this is the first time a multiscale scheme is used to model the mechanical behavior of a metal layer, which is supported by an elastomer substrate, in order to analyze the formability of the resulting metal/substrate bilayer. In the current analysis, the mechanical behavior of the elastomer layer is assumed to obey the hyperelastic neo-Hookean constitutive law. Also, the adherence between the two layers is assumed to be perfect. Consequently, the effect of interfacial

delamination between the two layers on the ductility of the bilayer cannot be analyzed within the current framework and will be the subject of a future investigation.

The remainder of the paper is organized as follows:

- The constitutive equations describing the mechanical behavior of the metal and elastomer layers will be outlined in the second Section.
- In the third Section, the theoretical framework for the two localization criteria will be presented.
- Various numerical results obtained by the application of the developed tool will be presented and discussed in the fourth Section.

Notations and nomenclature

The following notations and abbreviations are adopted in this paper:

- Mechanical fields corresponding to the polycrystal (resp. single crystal) scale are denoted by capital (resp. small) letters. To be consistent with the notations adopted for the metal layer, the different mechanical fields corresponding to the elastomer layer are also denoted by capital letters.
- $\bullet^{PS}$: the in-plane part of a given field $\bullet$ (in relation with the plane-stress assumption).
- $\bullet_{\blacklozenge}$: quantity $\bullet$ associated with layer $\blacklozenge$ (metal or elastomer layer).
- $\bullet(B)$: quantity $\bullet$ associated with the band (M–K analysis).
- $\bullet(S)$: quantity $\bullet$ associated with the safe zone (M–K analysis).
- $\bullet^{0}$: the initial value of quantity $\bullet$.

- FM (resp. BL), in figures of BPrediction results^ Section, refers to freestanding metal layer (resp. metal/elastomer bilayer).

These notations may be combined. For instance, tensor X in the elastomer layer of the band is denoted $X_E(B)$.

Mechanical behavior of the bilayer

Metal layer

Constitutive equations at the polycrystalline scale

Let us consider a polycrystalline aggregate, which is assumed to be statistically representative of the metal layer. The constitutive modeling of this aggregate is thus sufficient to accurately describe the mechanical behavior of the whole metal layer. To derive the constitutive law of the polycrystalline aggregate from that of its microscopic constituents, the Taylor model is used.

The constitutive modeling of the polycrystalline aggregate is achieved within the framework of finite strains. In the context of large deformations, several possible tangent moduli can be derived. These different choices are mainly dependent on the adopted stress and strain measures. In our case, we used the nominal stress rate $\dot{N}$ as appropriate stress measure to express the constitutive equations and the bifurcation relations. The nominal stress tensor N is defined as the transpose of the first Piola–Kirchhoff stress tensor. The strain measure, which is work-conjugate to the nominal stress rate $\dot{N}$, corresponds to the velocity gradient G. This choice is motivated by the formulation of the bifurcation equations proposed by Rudnicki and Rice [15], who demonstrated that the most appropriate formulation for the bifurcation theory at finite strains requires the choice of these work-conjugate variables. Indeed, the use of these work-conjugate variables allows the automatic satisfaction of the rate (incremental) form of both the equilibrium and the compatibility conditions. Further details on this choice are provided in [15] and [16]. The macroscopic tangent modulus L linking $\dot{N}$ to G is then obtained by using the Taylor model

$$\dot{N} = L : G \qquad (1)$$

According to the Taylor scale-transition scheme, the macroscopic velocity gradient G is assumed to be homogeneous over the polycrystalline aggregate:

$$\forall I = 1; \ldots; N_g : \quad G = g^I \qquad (2)$$

where N_g is the number of single crystals that compose the polycrystalline aggregate and g^I is the velocity gradient of grain I.

The macroscopic nominal stress rate $\dot{N}$ is related to its microscopic counterpart $\dot{n}$ by the following average relation:

$$\dot{N} = \frac{1}{V}\int_V \dot{n}(x)\,dx \qquad (3)$$

where x designates a material point within the polycrystalline aggregate.

In the same way, the macroscopic tangent modulus L is related to its microscopic counterpart l by a similar relationship:

$$L = \frac{1}{V}\int_V l(x)\,dx \qquad (4)$$

Therefore, to compute the macroscopic tangent modulus L via Eq. (4), the microscopic tangent modulus l of all individual grains should be first computed. To this end, the following Section is dedicated to the derivation of the analytical expression of the microscopic tangent modulus.

Constitutive equations at the single crystal scale

The mechanical behavior of the single crystals that make up the polycrystalline aggregate is described within a rate-

independent constitutive framework. Because the single crystals undergo finite strains, the effect of lattice rotation is accounted for.

At the microscopic level, a behavior law similar to Eq. (1) can be obtained by combining the constitutive relations of the single crystal:

$$\dot{n} = l : g \qquad (5)$$

The microscopic velocity gradient is additively split into its symmetric and skew-symmetric parts, denoted as d and w, respectively

$$d = (1/2)(g + g^T); \; w = (1/2)(g - g^T) \qquad (6)$$

The strain rate tensor d and the spin tensor w are split into their elastic and plastic parts

$$d = d^e + d^p; \; w = w^e + w^p \qquad (7)$$

The rotation r of the single crystal lattice frame is related to the elastic part of the spin tensor w^e by the following relation:

$$\dot{r}.r^T = w^e \qquad (8)$$

In order to satisfy the objectivity principle, the co-rotational rate σ^{∇} of the Cauchy stress tensor σ, with respect to the lattice rotation, is related to the elastic strain rate d^e by the following hypoelastic law:

$$\sigma^{\nabla} = \dot{\sigma} - w^e.\sigma + \sigma.w^e = C^e : d^e \qquad (9)$$

where C^e is the fourth-order elasticity tensor. The elastic behavior of the metal layer is assumed to be isotropic and therefore C^e is defined by the Young modulus E and the Poisson ratio ν.

The inelastic deformation is only due to the slip on the crystallographic planes. Thus, d^p and w^p can be defined by the following relations:

$$d^p = \sum_{\beta=1}^{N_s} \dot{\gamma}^\beta \, \mathrm{sgn}(\tau^\beta) R^\beta; \; w^p = \sum_{\beta=1}^{N_s} \dot{\gamma}^\beta \, \mathrm{sgn}(\tau^\beta) S^\beta \qquad (10)$$

where:

- N_s is the total number of slip systems (equal to 12 for FCC crystallographic structure).
- $\dot{\gamma}^\beta$ is the slip rate of the slip system β.
- R^β (resp. S^β) is the symmetric part (resp. skew-symmetric part) of the Schmid orientation tensor.
- τ^β is the resolved shear stress of the slip system β, which is equal to $\sigma : R^\beta$.

The Schmid law is used to model the plastic flow of the single crystal, as follows:

$$\forall \beta = 1; \ldots; N_s : \begin{cases} \tau^\beta < \tau_c^\beta \Rightarrow \dot{\gamma}^\beta = 0 \\ \tau^\beta = \tau_c^\beta \Rightarrow \dot{\gamma}^\beta \geq 0 \end{cases} \qquad (11)$$

where τ_c^β is the critical shear stress of the slip system β.

The Cauchy stress tensor σ is related to the nominal stress tensor n by the following relation:

$$n = j f^{-1}.\sigma \qquad (12)$$

where j is the Jacobian of the microscopic deformation gradient f.

The index form of Eq. (12) is given as follows:

$$n_{ij} = j f^{-1}_{ik} \sigma_{kj} \qquad (13)$$

The nominal stress rate $\dot{n}$ involved in Eqs. (3) and (5) can be easily obtained from Eq. (12)

$$\dot{n} = j f^{-1} : (\dot{\sigma} + \sigma \mathrm{Tr}(d) - g.\sigma) \qquad (14)$$

In the current paper, an updated Lagrangian approach is adopted. Thus, in Eq. (14), f is set to the second-order identity tensor I_2 and j is set to 1, which reduces to

$$\dot{n} = \dot{\sigma} + \sigma \mathrm{Tr}(d) - g.\sigma \qquad (15)$$

By combining Eqs. (6), (7), (9), (10) and (15), $\dot{n}$ can be expressed as a function of the slip rates $\dot{\gamma}^\beta$

$$\dot{n} = (C^e + \sigma \otimes I_2) : d - \sigma.w + d.\sigma - \sum_{\beta=1}^{N_s} \mathrm{sgn}(\tau^\beta)(C^e : R^\beta + S^\beta.\sigma - \sigma.S^\beta)\dot{\gamma}^\beta \qquad (16)$$

Let us now introduce the set of active slip systems A; defined as the slip systems for which the slip rates are strictly positive. The set of slip systems β used in Eq. (16) is then reduced to the set A

$$\dot{n} = (C^e + \sigma \otimes I_2) : d - \sigma.w + d.\sigma - \sum_{\beta \in A} \mathrm{sgn}(\tau^\beta)(C^e : R^\beta + S^\beta.\sigma - \sigma.S^\beta)\dot{\gamma}^\beta \qquad (17)$$

In order to obtain the expression of the microscopic tangent modulus l from relation (17), the slip rates $\dot{\gamma}^\beta$ of the active slip systems should be expressed as functions of g. To this end, the consistency condition, restricted to the active slip systems, is used

$$\forall \beta \in A : \dot{\chi}^\beta = \mathrm{sgn}(\tau^\beta)\dot{\tau}^\beta - \dot{\tau}_c^\beta = 0; \; \dot{\gamma}^\beta > 0 \qquad (18)$$

By using the definition of the resolved shear stress as well as Eqs. $(7)_1$ and (9), the resolved shear stress rate $\dot{\tau}^\beta$ can be expressed as

$$\forall \beta \in A : \dot{\tau}^\beta = R^\beta : \sigma^{\nabla} = R^\beta : C^e : (d - d^p) \qquad (19)$$

As to the time derivative of τ_c^β, it is given by the following isotropic hardening law:

$$\forall \beta \in A : \dot{\tau}_c^{\beta} = h \sum_{\alpha \in A} \dot{\gamma}^{\alpha}$$
$$h = h_0 \left(1 - \frac{h_0 \Gamma}{\tau_0 n}\right)^{n-1} ; \Gamma = \sum_{\alpha=1}^{N_s} \gamma^{\alpha} \quad (20)$$

where h_0 is the initial hardening rate and n the power-law hardening exponent. τ_0 is the initial critical shear stress, which is assumed to be the same for the different slip systems. It must be noted that the developed model and the corresponding numerical tools are not restricted to this particular hardening law, and can easily incorporate other hardening models.

The expression of the slip rates for the active slip systems is finally obtained by inserting Eqs. $(10)_1$, (19) and (20) into the consistency condition (18)

$$\forall \beta \in A : \dot{\gamma}^{\beta} = \sum_{\alpha \in A} M^{\beta\alpha} \operatorname{sgn}(\tau^{\alpha}) R^{\alpha} : C^e : d = y^{\beta} : d \quad (21)$$

where M is the inverse of matrix P of rank $\mathrm{Card}(A)$, which is defined by the following index form:

$$\forall \alpha, \beta \in A : P^{\alpha\beta} = \left(h - \operatorname{sgn}(\tau^{\alpha}) \operatorname{sgn}(\tau^{\beta})\right) R^{\alpha} : C^e : R^{\beta} \quad (22)$$

Combining Eqs. (5), (17) and (21), one can obtain the analytical expression of the microscopic tangent modulus l

$$l = C^e + \sigma \otimes I_2 - {}^1\Lambda(\sigma) - {}^2\Lambda(\sigma) - \sum_{\alpha \in A} \operatorname{sgn}(\tau^{\alpha}) (C^e : R^{\alpha} + S^{\alpha} : \sigma - \sigma : S^{\alpha}) \otimes y^{\alpha} \quad (23)$$

where ${}^1\Lambda$ and ${}^2\Lambda$ are fourth-order tensors that reflect the contribution of Cauchy stress convective terms

$${}^1\Lambda_{ijkl}(\sigma) = \frac{1}{2}\left(\delta_{lj}\sigma_{ik} - \delta_{kj}\sigma_{il}\right)$$
$${}^2\Lambda_{ijkl}(\sigma) = \frac{1}{2}\left(\delta_{ik}\sigma_{lj} + \delta_{il}\sigma_{kj}\right) \quad (24)$$

To incrementally integrate the constitutive equations, at the single crystal scale, over a typical time increment $[t_n, t_{n+1}]$, an implicit algorithm is used. This algorithm belongs to the family of ultimate algorithms (initially developed by Borja and Wren [17]), and is very similar to the one developed in [18]. By analyzing the above constitutive equations, one can easily notice that the determination of the set of active slip systems A, from the set of potentially active slip systems $P = \{\beta = 1; \ldots; N_s : |\tau^{\beta}(t_n)| = \tau_c^{\beta}(t_n)\}$, as well as the corresponding slip rates $\dot{\gamma}^{\beta}$ allows the computation of all other mechanical variables. To this end, a combinatorial search strategy, very similar to the one proposed in [19], is used to determine the set of active slip systems from the set of potentially active slip systems. This search strategy is carried out iteratively and, at each iteration, a subset of the set of potentially active slip systems is selected to be the set of active slip systems. The slip rates corresponding to the presumed set of active slip systems are computed by using Eq. (21). If matrix P (see Eq. (22)) is singular (which corresponds to the well-known indetermination problem), the pseudo-inversion technique is used to invert it and then to compute the slip rates of the active slip systems. For the other slip systems, belonging to the set of potentially active slip systems, their slip rates are assumed to be equal to zero. After this step, the Schmid law given by Eq. (11) is checked for all of the potentially active slip systems. If at least one constraint of this Schmid law is violated, then the assumed set is not an effective set of active slip systems and another set is selected. Once the different mechanical variables are updated, the microscopic tangent modulus l is computed by using Eq. (23).

Elastomer layer

In contrast to the metal layer, the mechanical behavior of the elastomer layer is assumed to be homogeneous and is modeled by a hyperelastic neo-Hookean law [20]. The formulation of this model allows linking the Cauchy stress tensor Σ to the left Cauchy–Green tensor V

$$\Sigma = q I_2 + \mu V^2 \quad (25)$$

where μ is the shear modulus, q an unknown hydrostatic pressure to be determined by applying the incompressibility constraint, and V is defined by the following relation:

$$V^2 = F \cdot F^T \quad (26)$$

with F being the deformation gradient tensor of the elastomer layer.

In the particular case of plane-stress state (which will be adopted in "Strain localization criteria" Section to apply the different localization criteria), the unknown hydrostatic pressure q is easily determined by using the plane-stress condition ($\Sigma_{33} = 0$):

$$q = -\mu V_{33} \quad (27)$$

Strain localization criteria

Let us consider a bilayer comprised of a metal layer M and an elastomer layer E (Fig. 1). We define an orthogonal Cartesian coordinate system $(\vec{x}_1; \vec{x}_2; \vec{x}_3)$, which is tied to the bilayer. The axes $\vec{x}_1$; $\vec{x}_2$ and $\vec{x}_3$ coincide with the rolling, transverse, and normal directions of the sheet, respectively. The two layers are assumed to be perfectly adhered and sufficiently thin. Consistent with several literature works and considering the thickness of the bilayer, the assumption of generalized plane stress is adopted in both localization criteria (namely the bifurcation theory and the initial imperfection approach). Hutchinson and Neale [21] have proven the validity of such an assumption in the case of thin structures (which is the case

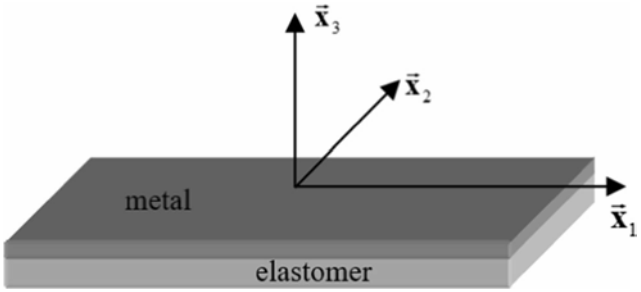

Fig. 1 Geometry of the bilayer and Cartesian coordinates

in the current study). The plane-stress conditions are expressed here in terms of out-of-plane components of the macroscopic nominal stress rate tensor $\dot{N}$ in both layers by:

$$\dot{N}_{13} = \dot{N}_{31} = \dot{N}_{23} = \dot{N}_{32} = \dot{N}_{33} = 0 \quad (28)$$

The numerical tools developed in the current paper are restricted to polycrystalline aggregates (which are assumed to be representative of the metal layer) with orthotropic initial texture. For this type of materials, the plane-stress assumption implies that the out-of-plane components of the macroscopic velocity gradient, in both layers, are equal to zero:

$$G_{13} = G_{31} = G_{23} = G_{32} = 0 \quad (29)$$

Bifurcation theory

Theoretical equations

The bilayer is submitted to uniform strain, where the in-plane strain rate components $\dot{E}_{11}$, $\dot{E}_{22}$ and $\dot{E}_{12}$ are equal to 1, ρ and 0, respectively. Parameter ρ designates the strain-path ratio, which ranges from $-1/2$ (uniaxial tensile state) to 1 (equibiaxial tensile state). Considering the plane-stress conditions, expressed by Eqs. (28) and (29), as well as the incompressibility of the elastomer layer, the above specific loading implies that the macroscopic velocity gradient and the macroscopic nominal stress rate tensor for both layers have the following generic forms:

$$G_M = \begin{pmatrix} 1 & 0 & 0 \\ 0 & \rho & 0 \\ 0 & 0 & ? \end{pmatrix}; \quad \dot{N}_M = \begin{pmatrix} ? & ? & 0 \\ ? & ? & 0 \\ 0 & 0 & 0 \end{pmatrix}$$
$$G_E = \begin{pmatrix} ? & ? & 0 \\ ? & \rho & 0 \\ 0 & 0 & -(1+\rho) \end{pmatrix}; \quad \dot{N}_E = \begin{pmatrix} ? & ? & 0 \\ ? & ? & 0 \\ 0 & 0 & 0 \end{pmatrix} \quad (30)$$

where symbol ? designates the unknown components in the above tensors. It must be noted that the components of tensor $\dot{N}$ are different from one layer to another (due to the difference in the mechanical behavior between the two layers).

The bifurcation criterion states that strain localization occurs when the acoustic tensor associated with the bilayer becomes singular (see, e.g., [7]). Hence, this criterion is expressed in the following form:

$$\det\left(\vec{N}^{PS} \cdot L^{PS} \cdot \vec{N}^{PS}\right) = 0 \quad (31)$$

where:

- $\vec{N}^{PS}$ is the unit vector (lying in the plane of the bilayer) normal to the localization band. Here, $\vec{N}^{PS}$ is taken equal to $(\cos\theta, \sin\theta)$.
- L^{PS} is the averaged plane-stress tangent modulus of the bilayer. This modulus is defined by the following relation:

$$L^{PS} = \frac{h_M L_M^{PS} + h_E L_E^{PS}}{h_M + h_E} \quad (32)$$

where h_M (resp. h_E) is the current thickness of the metal (resp. elastomer) layer and L_M^{PS} (resp. L_E^{PS}) is the plane-stress tangent modulus of the metal (resp. elastomer) layer.

L_M^{PS} is derived from the 3D expression of the metal layer tangent modulus L_M by using the following condensation relation:

$$\forall \alpha;\beta;\gamma;\delta = 1;2: \quad L^{PS}_{M\alpha\beta\gamma\delta} = L_{M\alpha\beta\gamma\delta} - \frac{L_{M\alpha\beta33}\, L_{M33\gamma\delta}}{L_{M3333}} \quad (33)$$

where L_M is determined by using the Taylor multiscale scheme described in BConstitutive equations at the polycrystalline scale^ Section. An iterative scheme is required to compute the 33 component of tensor G_M so that the plane-stress condition is fulfilled in the metal layer.

The plane-stress tangent modulus L_E^{PS} corresponding to the elastomer layer is directly determined by using the following relation [13]:

$$L_E^{PS} = \mathcal{L} + \Sigma \otimes I_2 - {}^1\Lambda(\delta\Sigma) - {}^2\Lambda(\delta\Sigma) \quad (34)$$

The generic forms of tensors ${}^1\Lambda$ and ${}^2\Lambda$ involved in relation (34) are given in Eq. (24).

The non-zero components of the fourth-order tensor $\mathcal{L}$ are defined by the following relations (see [14]):

$$\begin{cases} \mathcal{L}_{1111} = 2\mu\left[e^{2E_{11}} + e^{-2\delta E_{11}+E_{22}}\right] \\ \mathcal{L}_{2222} = 2\mu\left[e^{2E_{22}} + e^{-2\delta E_{11}+E_{22}}\right] \\ \mathcal{L}_{1122} = 2\mu e^{-2\delta E_{11}+E_{22}} \\ \mathcal{L}_{1212} = \frac{2\mu}{2}\left[e^{2E_{11}} + e^{2E_{22}}\right] \end{cases} \quad (35)$$

The current thicknesses h_M and h_E of the two layers are related to their initial values h_M^0 and h_E^0 by the following relations:

$$h_M = h_M^0 e^{\int G_{M33}\,dt} \quad ; \quad h_E = h_E^0 e^{-\nu(\Sigma_{11}+\Sigma_{22})} \qquad (36)$$

Algorithmic aspects

For each strain-path ratio ρ, and at each time increment, the tangent modulus L_E^{PS} is computed by using Eq. (34). For the same time increment, an iterative scheme is applied to determine the value of G_{M33}, which ensures the plane-stress condition in the metal layer. Once this iterative scheme has converged, the tangent modulus L_M^{PS} is determined by the condensation relation (33). Then, the layer thicknesses are updated by Eqs. (36) and the averaged tangent modulus of the bilayer L^{PS} is determined by Eq. (32). Once L^{PS} is obtained, the bifurcation criterion (31) is checked for all possible band orientations ($\theta \in [0, 90°]$). When the determinant of the acoustic tensor becomes negative for a given band orientation, then localized necking is detected. The associated angle θ corresponds to the orientation of the localization band, while the associated major strain E_{11} corresponds to the localization limit strain.

Initial imperfection approach

Theoretical equations

It has been experimentally observed that there are at least three main failure modes for thin substrate-supported metal layers: the plastic strain localization of the metal layer under biaxial stretching, the development of damage in the metal layer, and the buckling and the delamination under compression (see Refs. [22–24]). As has been discussed in the introduction, the second and third failure modes (namely, damage, buckling and delamination between layers) are not the matter of the current contribution, where the main focus is restricted to the prediction of the inception of localized necking in the bilayer. Hence, to accurately model this problem by using the imperfection approach (called hereafter M–K analysis for the sake of brevity), it is more convenient to introduce the initial geometric imperfection in the form of a band in the metal layer (Fig. 2). The introduction of this imperfection will ultimately trigger the initiation and development of localized necking in the whole bilayer. Note that this choice of introducing the initial imperfection in the metal layer has been followed and discussed earlier by Xue and Hutchinson (see, e.g., [12, 13]).

To clearly develop the equations of the M–K analysis related to the metal/elastomer bilayer, the following notations are adopted:

- $h_M^0(B)$ and $h_M(B)$: initial and current thickness, respectively, of the metal layer inside the band.

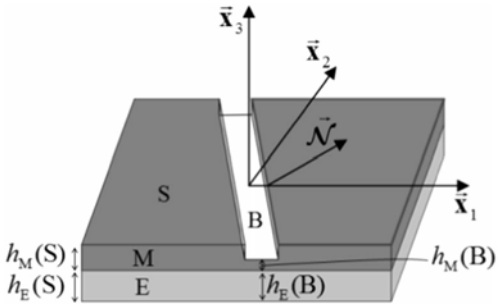

Fig. 2 M–K analysis for a bilayer (current geometry and band orientation)

- $h_M^0(S)$ and $h_M(S)$: initial and current thickness, respectively, of the metal layer outside the band.
- $h_E^0(B)$ and $h_E(B)$: initial and current thickness, respectively, of the elastomer layer inside the band.
- $h_E^0(S)$ and $h_E(S)$: initial and current thickness, respectively, of the elastomer layer outside the band.

Note that $h_E^0(S)$ and $h_E(S)$ are equal to $h_E^0(B)$ and $h_E(B)$, respectively.

On the basis of these notations, the initial geometric imperfection ratio ξ_0 (corresponding to the metal layer only) can be defined as

$$\xi_0 = 1 - \frac{h_M^0(B)}{h_M^0(S)} \qquad (37)$$

The M–K analysis is governed by four main sets of equations, which are specified in what follows:

- As a consequence of the perfect adherence between the metal and the elastomer layer, the following equalities between the in-plane velocity gradients in the metal layer and their counterparts in the elastomer layer are satisfied:

$$\begin{aligned} G_M^{PS}(B) &= G_E^{PS}(B) \\ G_M^{PS}(S) &= G_E^{PS}(S) \end{aligned} \qquad (38)$$

When the adherence between the two layers is not perfect, the above equalities between the in-plane velocity gradients in the metal and elastomer layers are not satisfied. In this case, the beneficial effect of necking retardation due to the elastomer layer is reduced to some extent, which should be proportional to the extent of surface debonding.

- The kinematic compatibility condition between the band and the uniform zone (i.e., outside the band): this condition requires the displacement increments to be continuous across the band, and it is mathematically expressed as

tively, of the metal layer inside the band. $G^{PS}(B) = G^{PS}(S) + C^{PS}\otimes$

→ ð39Þ PS
N

- The equilibrium balance across the interface between the band and the homogeneous zone:

$$\vec{N}^{PS}_{S} : h_M(B)\dot{N}^{PS}_{M}(B) + h_E(B)\dot{N}^{PS}_{E}(B) = \vec{N}^{PS} : h_M(S)\dot{N}^{PS}_{M}(S) + h_E(S)\dot{N}^{PS}_{E}(S) \quad (40)$$

- The behavior law of both the metal and the elastomer layer, restricted to the plane dimension, inside and outside the band, respectively: these constitutive equations are expressed in the following generic form:

$$\begin{aligned} \dot{N}^{PS}_{M}(B) &= L^{PS}_{M}(B) : G^{PS}(B); \\ \dot{N}^{PS}_{E}(B) &= L^{PS}_{E}(B) : G^{PS}(B) \\ \dot{N}^{PS}_{M}(S) &= L^{PS}_{M}(S) : G^{PS}(S); \\ \dot{N}^{PS}_{E}(S) &= L^{PS}_{E}(S) : G^{PS}(S) \end{aligned} \quad (41)$$

By inserting the constitutive relations (41) into the equilibrium eq. (40), this latter becomes

$$\vec{N}^{PS} : \left(h_M(B)L^{PS}_{M}(B) + h_E(B)L^{PS}_{E}(B)\right) : G^{PS}(B) = \vec{N}^{PS} : \left(h_M(S)L^{PS}_{M}(S) + h_E(S)L^{PS}_{E}(S)\right) : G^{PS}(S) \quad (42)$$

In other words, Eq. (42) is equivalent to:

$$\vec{N}^{PS} : L^{PS}(B) : G^{PS}(B) = \vec{N}^{PS} : L^{PS}(S) : G^{PS}(S) \quad (43)$$

where $L^{PS}(B)$ and $L^{PS}(S)$ are defined by the following relations:

$$\begin{aligned} L^{PS}(B) &= h_M(B)L^{PS}_{M}(B) + h_E(B)L^{PS}_{E}(B) \\ L^{PS}(S) &= h_M(S)L^{PS}_{M}(S) + h_E(S)L^{PS}_{E}(S) \end{aligned} \quad (44)$$

Combining the compatibility condition (39) and the equilibrium eq. (43), one can derive the following expression for the jump vector $\dot{\vec{C}}^{PS}$:

$$\dot{\vec{C}}^{PS} = \left(\vec{N}^{PS} : L^{PS}(B) : \vec{N}^{PS}\right)^{-1} \left(\vec{N}^{PS} : \left(L^{PS}(S) - L^{PS}(B)\right) : G^{PS}(S)\right) \quad (45)$$

From the above equations (see, e.g., Eq. (39)), it is clear that the localization of deformation occurs when the magnitude of vector $\dot{\vec{C}}^{PS}$ becomes very large, which means that the velocity gradient in the band $G^{PS}(B)$ becomes very large as compared to that in the safe zone $G^{PS}(S)$. In such a situation, the deformation concentrates much more rapidly in the imperfection zone than in the safe zone. A natural outcome from

$$\left\|\dot{\vec{C}}^{PS}\right\| \to \infty \Leftrightarrow \det\left(\vec{N}^{PS} : L^{PS}(B) : \vec{N}^{PS}\right) \to 0 \quad (46)$$

Comparing the above equation with the bifurcation criterion given by Eq. (31), it is reasonable to expect that the limit strains predicted by the initial imperfection approach tend to those obtained by the bifurcationtheory when the initial imperfection ratio f_0 tends towards zero. This observation will be verified in BPrediction results^ Section on the basis of various numerical predictions.

Algorithmic aspects

For each strain-path ratio ρ, and each initial band orientation θ_0, the equations that govern the M–K analysis are incrementally integrated over each time increment. Indeed, by analyzing Eq. (45), it can be seen that the main incremental unknown of the M–K approach is the jump vector $\dot{\vec{C}}^{PS}$. This jump vector is determined at the end of the time increment by using the fixed point iterative method. For each loading case (i.e., a given strain-path ratio ρ and a given initial band orientation θ_0), the computations are conducted until the norm of the jump vector $\dot{\vec{C}}^{PS}$ increases abruptly. For the complete details on the numerical and algorithmic aspects regarding the M–K approach, the reader may refer to [14].

Prediction results

Material and geometric data

Several studies, mainly based on some statistical techniques, have been carried out in the literature to evaluate the minimum number of grains that should be used to ensure the representativeness of the volume element. These studies reveal that the obtained results may depend on the boundary conditions applied on the polycrystalline aggregates (periodic boundary conditions….) as well as on the degree of anisotropy of the studied single crystals. In most references (see, for instance, Refs. [25, 26]), the number of grains required to ensure the representativeness of the volume element does not exceed

(45) is that the magnitude of vector C^{PS} becomes very large

1000. Accordingly, we have chosen a polycrystal with 2000
grains, considering that this number is sufficient to generate a volume element representative of the studied sheets. Indeed, from a variety of numerical experiments, we have observed that beyond 2000 grains, the response of the when $\vec{N}^{PS}:L^{PS}\delta B\Phi:\vec{N}^{PS}$ approaches singularity:

polycrystalline aggregate representing the metal layer remains almost un- changed. The initial texture corresponding to this aggregate is generated randomly (see Fig. 3), in such a way that it is orthotropic with respect to the rolling and transverse direc-
tions. It is widely recognized that the initial crystallographic texture strongly affects both the shape and the overall level of

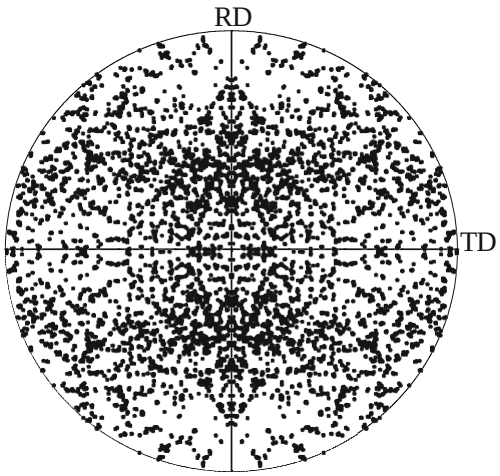

Fig. 3 Initial crystallographic texture of the studied polycrystalline aggregate: {111} pole figure

the predicted FLDs [27]. Initially, all of the grains are assumed to have the same volume fraction. We also assume that the adopted polycrystalline aggregate is representative of the studied metal sheet. As plastic strain localization occurs at relatively large strains, the values of the predicted limit strains are almost unaffected by the elastic behavior. This justifies the consideration of simple isotropic elastic behavior in the current study.

The material parameters of the single crystals are given in Table 1. They are the same as those used in [27].

The shear modulus of the elastomer layer is set to 22 MPa. This choice is based on data for polyurea [28]. To investigate the impact of the addition of the elastomer substrate on the formability of the bilayer, three values of the ratio of elastomer initial thickness to metal initial thickness are considered. The values taken for this ratio (denoted R in the subsequent simulation results) are: 0 (which corresponds to a freestanding metal layer), 1 and 2.

Bifurcation theory predictions

The predictions obtained by applying the bifurcation theory are presented and discussed in the current Section.

Before studying the effect of the addition of the elastomer substrate on the formability of the bilayer, we first analyze the evolution of three representative components (components 1111, 1122 and 1221) of the tangent moduli of both layers for the uniaxial tensile state ($\rho = -0.5$) and the equibiaxial tensile state ($\rho = 1$). These evolutions are shown in Fig. 4. From this figure, one can easily observe that the different components of L_M^{PS} steadily decrease for both strain paths investigated (especially for the equibiaxial tensile state). One particularly observes that the shearing component $L_{M\,1221}^{PS}$ is significantly reduced during the deformation and becomes very small. This observation is a natural outcome of the multi-slip character of crystal plasticity, which leads to the formation of vertices at the current points of the Schmid yield surfaces of single crystals. The reduction of these shearing components is the main destabilizing factor responsible for bifurcation, thus promoting early plastic strain localization (see, e.g., [29, 30]). A correlation can be easily established between the evolution of the shearing components of the tangent modulus and the corresponding limit strains predicted by bifurcation theory. It is worth noting that, when a smooth yield function is used, the shearing components of the tangent modulus keep practically a constant magnitude during the deformation (see, e.g., [14]). Contrary to the metal layer, the shearing component of the tangent modulus L_E^{PS} corresponding to the elastomer layer continuously increases during the deformation, as demonstrated in Fig. 4c and d. Note that this result is valid for the whole range of strain paths, and is not restricted to the particular strain paths investigated in Fig. 4. Considering the evolution of the shearing component L_{ET221}^{PS}, one can conclude that localized necking can never occur in the elastomer layer alone. In the same way, one may also expect a beneficial effect (in terms of retardation of localized necking) from the addition of an elastomer substrate.

It may also be noted that the components of L_E^{PS} evolve smoothly during the deformation, in contrast to the components of L_M^{PS}. Indeed, the tangent modulus L_M^{PS} of the metal layer is derived from the tangent moduli of the different constituent grains, using the averaging rule given by Eq. (4). In the current micromechanical constitutive modeling, the grains deform freely and the interactions between the different grains are obviously neglected. Consequently, the microscopic tangent modulus differs significantly from one grain to another, thus exhibiting high contrast in its components due to texture evolution. This high contrast results in a rather complex evolution for the components of the macroscopic tangent modulus, as demonstrated in Fig. 4a and b.

The effect of adding an elastomer substrate on the evolution of the minimum of the cubic root of the determinant of the acoustic tensor $N^{PS}:L^{PS}:N^{PS}$, over all possible band orientations, is illustrated in Fig. 5. The onset of strain localization is predicted when this minimum reaches 0, as defined by the bifurcation criterion (31). Four representative strain paths are considered in this figure: $\rho = -0.5$, $\rho = 0$, $\rho = 0.5$, and $\rho = 1$. By comparing the different evolutions displayed in Fig. 5, one can clearly observe that the presence of the elastomer layer

Table 1 Material parameters of the single crystals that make up the polycrystalline aggregate representative of the metal layer

Elasticity		Hardening		
E [GPa]	v	τ_0 [MPa]	h_0 [MPa]	n
65	0.3	40	390	0.35

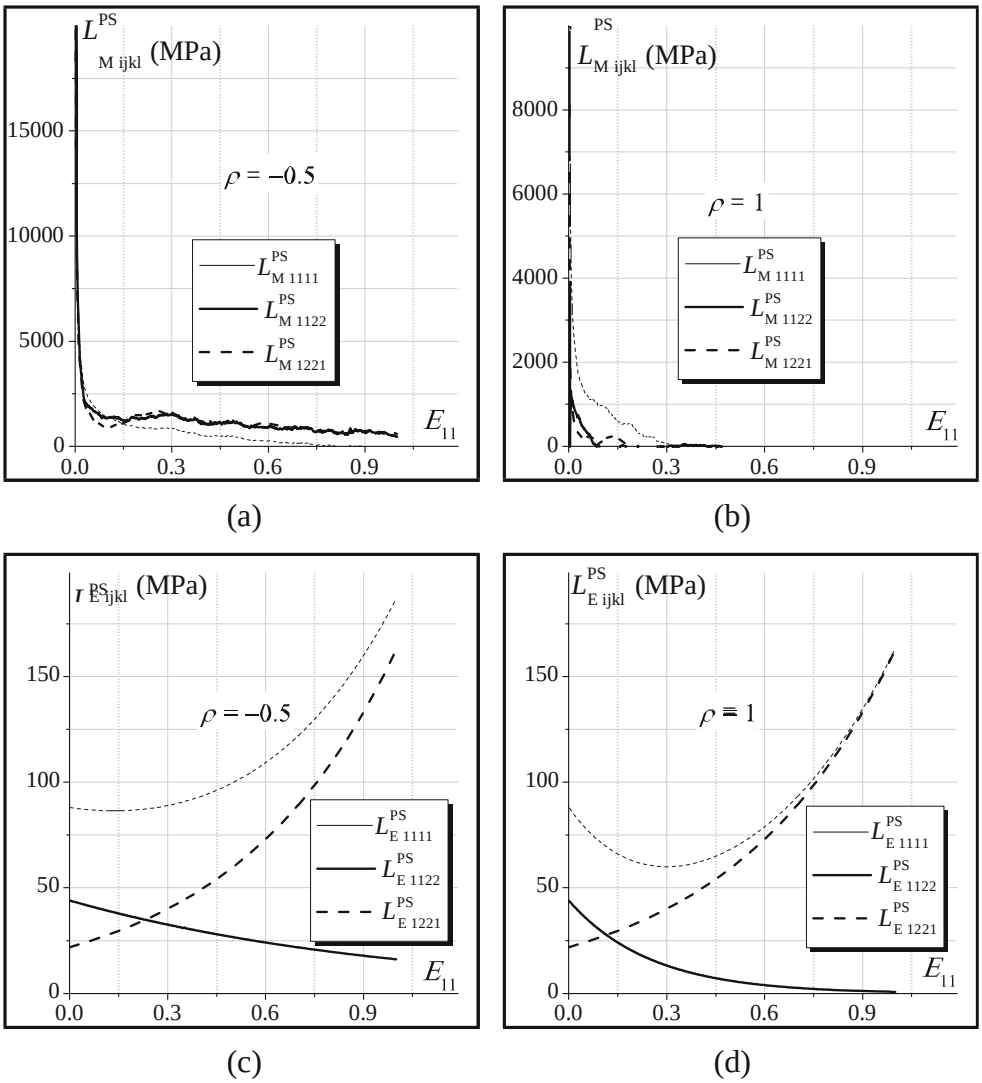

Fig. 4 Evolution of three representative components of L^{PS}_{M} and L^{PS}_{E} for two different strain paths ($\rho = -0.5$ and $\rho = 1$): a Metal layer ($\rho = -0.5$); b Metal layer ($\rho = 1$); c Elastomer layer ($\rho = -0.5$); d Elastomer layer ($\rho = 1$)

substantially retards the occurrence of strain localization. This result is expectable considering the evolution of the different components of L^{PS}_{M} and L^{PS}_{E} investigated in Fig. 4. This necking retardation, due to the addition of the elastomer substrate, is particularly clear in Fig. 5a, where bifurcation is still not detected for the thickness ratio $R = 2$, while the computations are stopped at a strain value of $E_{11} = 1$.

The effect of the elastomer substrate on necking retardation for the whole range of strain paths ($\rho \in [-1/2, 1]$) is shown in Fig. 6. This figure, confirms the preliminary results obtained in Fig. 5: namely, the addition of an elastomer layer allows shifting the FLD upwards, especially in the negative range of strain paths, and thus a significant enhancement in the ductility of the bilayer.

Figure 7 provides additional details and better explains the effect of the relative thickness R of the elastomer layer on the ductility limit of the bilayer. In this figure, the beneficial effect of the thickness ratio R on the enhancement of ductility of the bilayer is confirmed once again. From this figure, it is clearly shown that the limit strain E_{11} increases slowly and almost linearly with the initial thickness ratio R, for the different strain paths considered, except in the case $\rho = -0.5$, where the limit strain increases more rapidly. The same trends have been obtained when the flow theory of plasticity is used (instead of the micromechanical Taylor model) to model the mechanical behavior of the metal layer, as demonstrated in [14]. Also, further relevant details and explanations on the evolution of the limit strain, as a function of the initial thickness ratio R, for various strain paths are provided in [14].

M–K analysis predictions

In this Section, the formability of both the freestanding metal layer and the metal/elastomer bilayer is predicted by using the initial imperfection approach. The results of this Section may be viewed as an extension of the results reported in Fig. 6. In the different simulations, which will be presented in the current Section, two different values for the initial geometric imperfection ratio ξ_0 are used: 10^{-3} and 10^{-2}. Figure 8

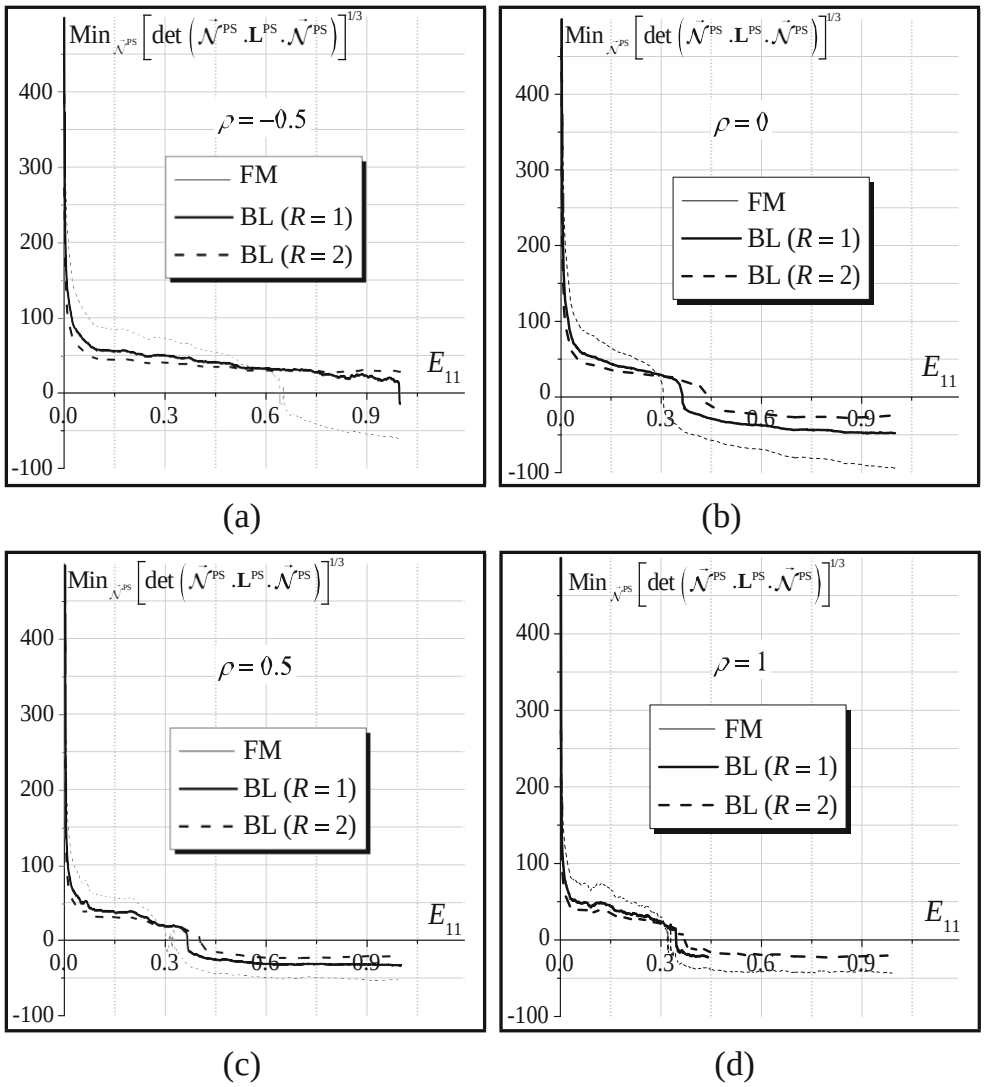

Fig. 5 Effect of adding an elastomer substrate on the evolution of the minimum of the cubic root of the determinant of the acoustic tensor as a function of E_{11}: a $\rho = -0.5$; b $\rho = 0$; c $\rho = 0.5$; d $\rho = 1$

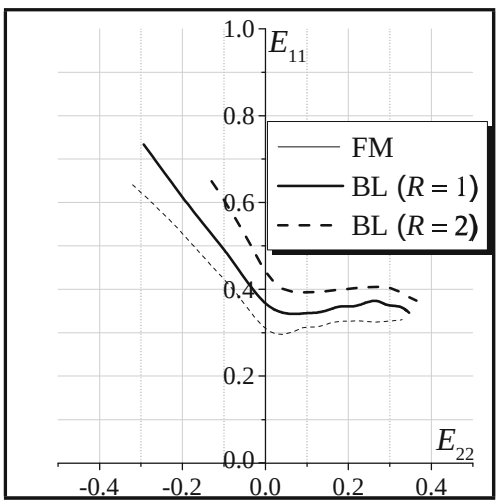

Fig. 6 Effect of the elastomer substrate on the improvement of the formability of the bilayer (predictions based on bifurcation theory)

illustrates the effect of the addition of an elastomer layer on the formability of the bilayer, as predicted by the initial imperfection approach. The results of this figure confirm the observations made in the previous Section, where the bifurcation theory has been used: namely, the elastomer substrate allows the formability of the bilayer to be enhanced. This observation is common to both initial imperfection ratios (namely, $\xi_0=10^{-3}$ and $\xi_0=10^{-2}$). It is also shown that the effect of the elastomer substrate is more significant in the range of negative strain paths.

The limit strains obtained by applying the bifurcation analysis set an upper bound to those yielded by the M–K approach. Indeed, Fig. 9 demonstrates that the FLDs predicted by the M–K approach tend towards the FLD predicted by bifurcation analysis when the initial imperfection ratio ξ_0 tends to zero. In other words, the effect of an initial imperfection is essentially to shift the FLD downwards. This observation is natural considering the similarity of the

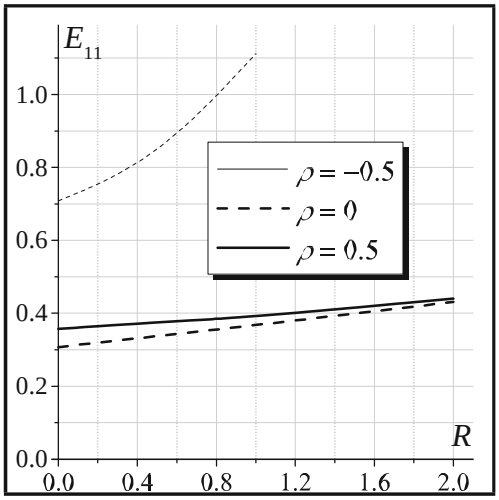

Fig. 7 Effect of the relative thickness of the elastomer layer on the enhancement of ductility of the bilayer (predictions based on bifurcation theory)

mathematical formulations of the two approaches (M−K and bifurcation): if the amount of initial imperfection is set to 0 in the imperfection model, the problem reduces to the bifurcation analysis. This conclusion is valid for a freestanding metal layer as well as for an elastomer-supported metal layer.

As demonstrated in Fig. 9, an increase in the amount of initial imperfection leads to a reduction in the limit strains. To further illustrate this feature, Fig. 10 shows the evolution of the limit strain E_{11} as a function of the initial imperfection size ξ_0 for different strain-path ratios ρ. Note that, in this figure, the limit strain corresponding to the abscissa $\xi_0 = 0$ is the one predicted by the bifurcation criterion. It can be clearly seen that the limit strain decreases when the initial imperfection increases, for all strain-path ratios ρ investigated. This dependence of the predicted limit strains on the amount of initial imperfection has been previously studied using multiscale rate-dependent approaches (see [31, 32]) or rate-independent crystal plasticity modeling (see [27]). The results obtained in the present study are in agreement with those reported in the above literature studies.

Computation times

The numerical tools pertaining to the current study have been implemented using the multi-paradigm numerical computing environment Matlab (R2015). This choice is motivated by the fact that this software offers efficient and powerful tools and functionalities in order to optimize the numerical implementation. The simulations presented in this paper are all performed on a personal computer with 2.00 GHz of CPU frequency and 6.00 Go of RAM memory. The CPU time required for the prediction of a single FLD by using the bifurcation theory (resp. the initial imperfection approach) is about 6400 s (resp. 60,000 s). Of course, the evaluation of these computation times is indicative and it is strongly dependent on a number of numerical parameters and choices (the increment for the strain-path ratio, the increment selected for the band orientation angle when the initial imperfection approach is used, the size of the strain step used to integrate the constitutive equations corresponding to both the metal and elastomer layers, etc.).

Concluding remarks

A numerical tool to predict the onset of localized necking in substrate-supported metal layers has been developed in this paper. In this tool, the mechanical behavior of the metal (resp. elastomer) layer is modeled by the full-constraint Taylor multiscale model (resp. neo-Hookean hyperelastic model). The layers composing the bilayer remain bounded and are

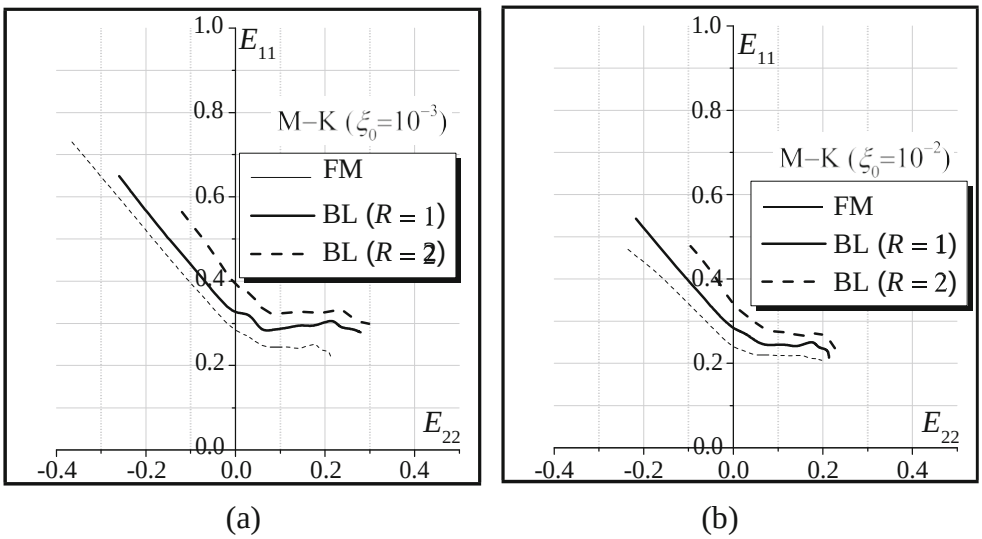

Fig. 8 Effect of the elastomer substrate on the improvement of the formability of the bilayer (predictions based on the M−K analysis): a $\xi_0 = 10^{-3}$; b $\xi_0 = 10^{-2}$

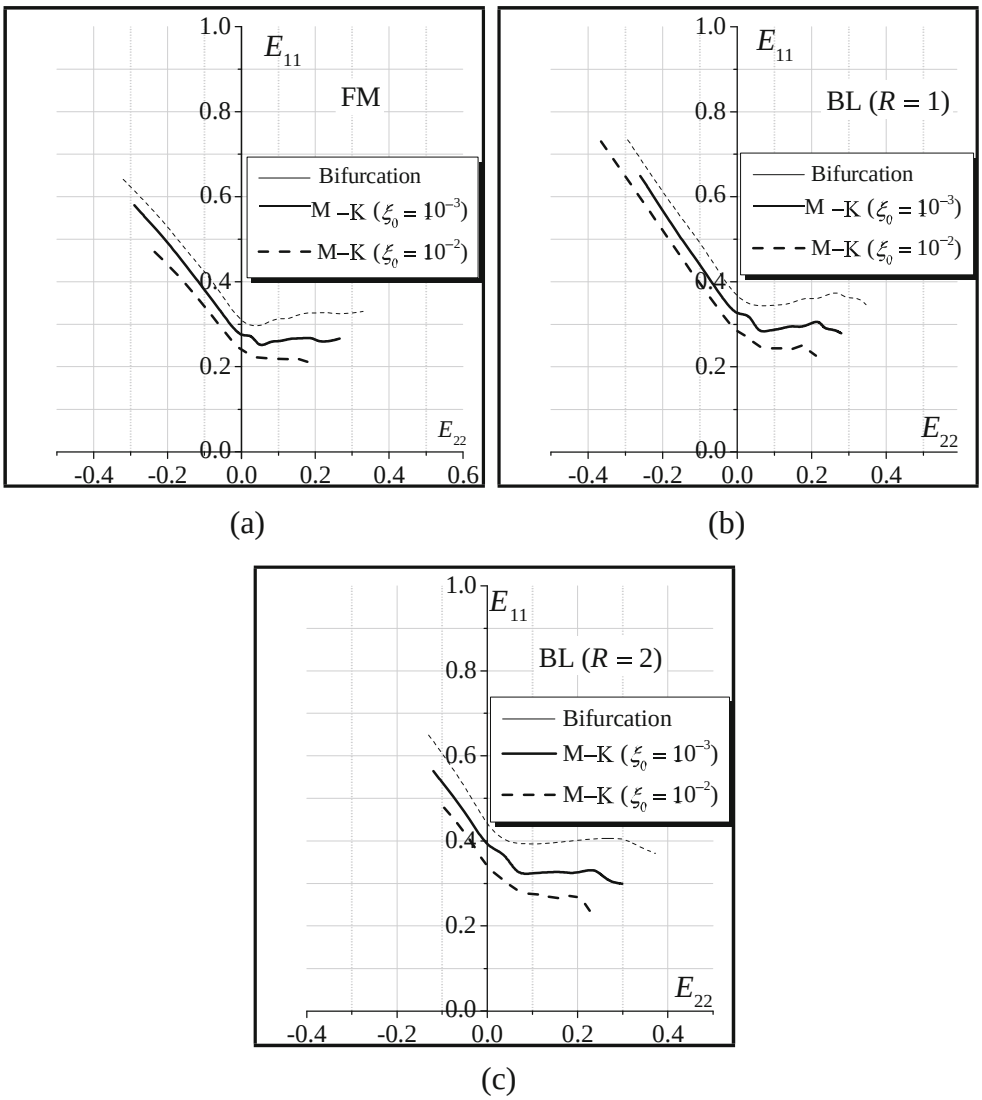

Fig. 9 Effect of the initial geometric imperfection on the shape and the level of the FLDs of the bilayer: a FM; b BL (R = 1); c BL (R = 2)

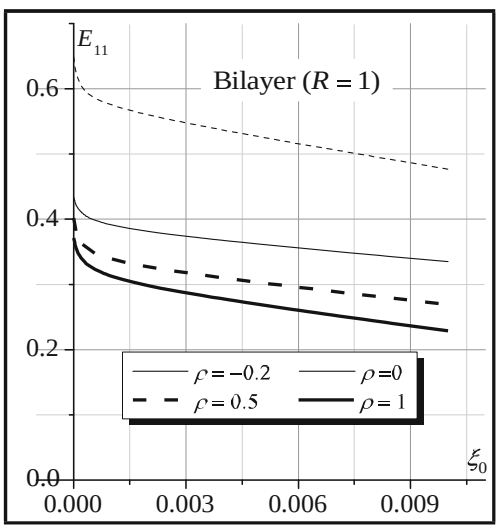

Fig. 10 Evolution of the limit strain E_{11}, as a function of the initial imperfection ratio ξ_0, for different strain-path ratios ρ

such that material damage does not occur prior to localized necking. Hence, other failure modes than localized necking (such as damage, interfacial delamination) are not considered in this contribution. The constitutive modeling of the bilayer is coupled with two strain localization criteria in order to predict the associated limit strains. These localized necking criteria consist of the bifurcation theory and the initial imperfection approach. From the numerical predictions obtained by applying this tool, three main conclusions can be drawn:

- The presence of an elastomer layer substantially increases the level of the limit strains for the bilayer.
- The shape and the level of the predicted FLDs are significantly influenced by the amount of initial geometric imperfection, which is assumed to initiate in the metal layer.
- The limit strains of the bilayer predicted by bifurcation theory set an upper bound to those yielded by the M−K approach.

It is worth noting that the use of the Taylor multiscale model in the current work has been mainly motivated by its simplicity and its efficiency. Indeed, with this scale-transition scheme, all the numerical results (for both freestanding metal layers and metal/elastomer bilayers), as well as the associated FLDs are obtained within reasonable running times. Also, we believe that the observed trends and the associated conclusions are valid whatever the multiscale scheme used.

From a practical perspective, the numerical tools developed in the current investigations can be used, in an industrial context, to provide guidelines and assistance in the design of new generations of electronic devices with improved ductility.

Compliance with ethical standards

Conflict of interest The authors declare that they have no conflict of interest.

References

1. Tekoğlu C, Hutchinson JW, Pardoen T (2015) On localization and void coalescence as a precursor to ductile fracture. Phil Trans R Soc A 373:2038
2. K. Saanouni (2012) Damage mechanics in metal forming. Advanced modeling and numerical simulation. ISTE/Wiley, London
3. Keeler SP, Backofen WA (1963) Plastic instability at fracture in sheets stretched over rigid punches. Trans ASM 56:25
4. Goodwin GM (1968) Application of the strain analysis to sheet metal forming in the press shop. Metallurgia Italiana 60:767
5. Kotkunde N, Krishna G, Shenoy SK, Gupta AK, Singh SK (2015) Experimental and theoretical investigation of forming limit diagram for Ti-6Al-4 V alloy at warm condition. Int J Mater Form 10(2): 255–266. https://doi.org/10.1007/s12289-015-1274-3
6. Strano M, Colosimo BM (2006) Logistic regression analysis for experimental determination of forming limit diagrams. Int J Mach Tool Manu 46(6):673–682. https://doi.org/10.1016/j.ijmachtools.2005.07.005
7. Rice JR (1976) The localization of plastic deformation. The localization of plastic deformation. In: Koiter W T (ed) Theoretical and Applied Mechanics (Proceedings of the 14th International Congress on Theoretical and Applied Mechanics, Delft, vol 1. North-Holland Publishing Co., Amsterdam, pp 207–220
8. Marciniak Z, Kuczynski K (1967) Limit strains in the processes of stretch-forming sheet metal. Int J Mech Sci 9(9):609–620. https://doi.org/10.1016/0020-7403(67)90066-5
9. Chiu SL, Leu J, Ho PS (1994) Fracture of metal-polymer line structures. I. Semiflexible polyimide. J Appl Phys 76(9):5136–5142. https://doi.org/10.1063/1.357227
10. Hommel M, Kraft O (2001) Deformation behavior of thin copper films on deformable substrates. Acta Mater 49(19):3935–3947. https://doi.org/10.1016/S1359-6454(01)00293-2
11. Alaca BE, Saif MTA, Sehitoglu H (2002) On the interface debond at the edge of a thin film on a thick substrate. Acta Mater 50(5): 1197–1209. https://doi.org/10.1016/S1359-6454(01)00421-9
12. Xue ZY, Hutchinson JW (2007) Neck retardation and enhanced energy absorption in metal–elastomer bilayers. Mech Mater 39(5): 473–487. https://doi.org/10.1016/j.mechmat.2006.08.002
13. Xue ZY, Hutchinson JW (2008) Neck development in metal/elastomer bilayers under dynamic stretchings. Int J Solids Struct 45(13):3769–3778. https://doi.org/10.1016/j.ijsolstr.2007.10.006
14. Ben Bettaieb M, Abed-Meraim F (2015) Investigation of localized necking in substrate-supported metal layers: Comparison of bifurcation and imperfection analyses. Int J Plast 65:168–190. https://doi.org/10.1016/j.ijplas.2014.09.003
15. Rudnicki JW, Rice JR (1975) Conditions for the localization of 937 deformation in pressure-sensitive dilatant materials. J. Mech. 938 Phys. Solids 23(6):371–394. https://doi.org/10.1016/0022-5096(75)90001-0
16. J.W. Hutchinson, K.W. Neale (1978) Sheet Necking- II. Time-Independent Behavior. In: Koistinen DP, Wang NM (eds) Mechanics of sheet metal forming. Plenum Publishing Corporation, New York, pp 127–153
17. Borja RI, Wren JR (1993) Discrete micromechanics of elastoplastic crystals. Int J Numer Methods Eng 36(22):3815–3840. https://doi.org/10.1002/nme.1620362205
18. Akpama HK, Ben Bettaieb M, Abed-Meraim F (2016) Numerical integration of rate-independent BCC single crystal plasticity models: comparative study of two classes of numerical algorithms. Int J Numer Methods Eng 108(5):363–422. https://doi.org/10.1002/nme.5215
19. Anand L, Kothari M (1996) A computational procedure for rate-independent crystal plasticity. J Mech Phys Solids 44(4):525–558. https://doi.org/10.1016/0022-5096(96)00001-4
20. Hunter SC (1979) Some exact solutions in the theory of finite elasticity for incompressible neo-Hookean materials. Int J Mech Sci 21(4):203–211. https://doi.org/10.1016/0020-7403(79)90064-X
21. Hutchinson JW, Neale KW, Needleman A (1978) Sheet Necking- I. Time-independent behavior. In: Koistinen DP, Wang N-M (eds) Mechanics of sheet metal forming, Plenum Publishing Corporation, New york, pp 111–126
22. Changchun Z, Hongpo Z, Jianqiang H, Wanzhao C (2003) MEMS Devices Technol. 10 (30)(2003)
23. McShane GJ, Stewart C, Aronson MT, Wadley HNG, Fleck NA, Deshpande VS (2008) Dynamic rupture of polymer–metal bilayer plates. Int J Solids Struct 45(16):4407–4426. https://doi.org/10.1016/j.ijsolstr.2008.03.017
24. Men Y, Wang S, Jia H, Wu Z, Li L, Zhang C (2013) Experimental study on tensile bifurcation of nanoscale Cu film bonded to polyethylene terephthalate substrate. Thin Solid Films 548:371–376. https://doi.org/10.1016/j.tsf.2013.08.090
25. Szyndler J, Madej L (2014) Effect of number of grains and boundary conditions on digital material representation deformation under plane strain. Arch Civ Mech Eng 14(3):360–369. https://doi.org/10.1016/j.acme.2013.09.001
26. Houdaigui FE, Forest S, Gourgues A-F, Jeulin D (2007) On the size of the representative volume element for isotropic elastic polycrystalline copper. In: Bai Y (ed) IUTAM Symposium on mechanical behavior and micro-mechanicsof nanostructured materials. Springer, Dordrecht pp 171–180
27. Yoshida K, Kuroda M (2012) Comparison of bifurcation and imperfection analyses of localized necking in rate-independent polycrystalline sheets. Int J Solids Struct 49(15-16):2073–2084. https://doi.org/10.1016/j.ijsolstr.2012.04.010
28. Amirkhizi AV, Isaacs J, McGee J, Nemat-Nasser S (2006) An experimentally-based viscoelastic constitutive model for polyurea, including pressure and temperature effects. Philos Mag 86(36): 5847–5866. https://doi.org/10.1080/14786430600833198
29. Hutchinson JW (1970) Elastic-Plastic Behaviour of Polycrystalline Metals and Composites. Proc R Soc Lond A 319(1537):247–272. https://doi.org/10.1098/rspa.1970.0177
30. Yoshida K, Brenner R, Bacroix B, Bouvier S (2009) Effect of regularization of Schmid law on self-consistent estimates for rate-

independent plasticity of polycrystals. Eur J Mech − A/Solids 28(5): 905−915. https://doi.org/10.1016/j.euromechsol.2009.05.001
31. Zhou Y, Neale KW (1995) Predictions of forming limit diagrams using a rate-sensitive crystal plasticity model. Int J Mech Sci 37(1): 1−20. https://doi.org/10.1016/0020-7403(94)00052-L
32. Signorelli JW, Bertinetti MA, Turner PA (2009) Predictions of forming limit diagrams using a rate-dependent polycrystal self-consistent plasticity model. Int J Plast 25(1):1−25. https://doi.org/10.1016/j.ijplas.2008.01.005